# Serveur Académique Lausannois SERVAL serval.unil.ch

# Author Manuscript

# UNIL | Faculty of Biology and Medicine Publication

This paper has been peer-reviewed but does not include the final publisher proof-corrections or journal pagination.

## Published in final edited form as:

**Free-running 5D coronary MR angiography at 1.5T using LIBRE water excitation pulses**

AUTHORS: Nemanja Masala[1], Jessica A.M. Bastiaansen[1], Lorenzo Di Sopra[1], Christopher W. Roy[1], Davide Piccini[1,2], Jérôme Yerly[1,3], Roberto Colotti[1], Matthias Stuber[1,3].

AFFILIATIONS:
1. Department of Diagnostic and Interventional Radiology, Lausanne University Hospital (CHUV) and University of Lausanne (UNIL), Lausanne, Switzerland.
2. Advanced Clinical Imaging Technology, Siemens Healthcare AG, Lausanne, Switzerland.
3. Center for Biomedical Imaging (CIBM), Lausanne, Switzerland.

Word count (excluding title page, abstract, figure captions, tables, table captions, or references): 6047

Abstract word count: 249

8 figures, 2 tables, 2 supporting information videos, 2 supporting information figures

# ABSTRACT

**Purpose**

To implement, optimize, and characterize lipid-insensitive binomial off-resonant RF excitation (LIBRE) pulses for fat-suppressed fully self-gated free-running 5D cardiac MRI.

**Methods**

Bloch equation simulations were used to optimize LIBRE parameter settings in non-interrupted bSSFP prior to in vitro validation. Thus, optimized LIBRE pulses were subsequently applied to free-running coronary MRA in 20 human adult subjects, where resulting images were quantitatively compared to those obtained with non-fat-suppressing excitation (SP), conventional 1-2-1 water excitation (WE), and a previously-published interrupted free-running (IFR) sequence. SAR and scan times were recorded. Respiratory-and-cardiac-motion-resolved images were reconstructed with XD-GRASP, and contrast ratios, coronary artery detection rate, vessel length, and vessel sharpness were computed.

**Results**

The numerically-optimized LIBRE parameters were successfully validated in vitro. In vivo, LIBRE had the lowest SAR and a scan time that was similar to that of WE yet 18% shorter than that of IFR. LIBRE improved blood-fat contrast when compared to SP, WE and IFR, vessel detection relative to SP and IFR, and vessel sharpness when compared to WE and IFR (for example, for the left main and anterior descending coronary artery, $51.5\% \pm 10.2\%$ (LIBRE) vs $42.1\% \pm 6.8\%$ (IFR)). Vessel length measurements remained unchanged for all investigated methods.

**Conclusion**

LIBRE enabled fully self-gated non-interrupted free-running 5D bSSFP imaging of the heart at 1.5T with suppressed fat signal. Measures of image quality, vessel conspicuity, and scan time compared favorably to those obtained with the more conventional non-interrupted WE and the previously-published interrupted free-running IFR, while SAR reduction offers added flexibility.

## INTRODUCTION

Cardiovascular disease accounts for $350 billion in direct and indirect healthcare costs annually in the United States of America, and accounts for more deaths than any other disease, with coronary artery disease (CAD) being the leading cause of cardiovascular disease-related deaths (1). The gold standard for assessing CAD, x-ray coronary angiography, is invasive, uses ionizing radiation, and poses a small risk of complications (2). Coronary magnetic resonance angiography (CMRA) is a potential alternative with several advantages: no ionizing radiation, high spatial resolution in all three dimensions, and high soft-tissue contrast (2,3). Recent CMRA approaches have used 3D whole-heart protocols (4), for adequate volumetric coverage, with ECG triggering in mid-diastole to account for cardiac motion, and both respiratory navigators (4) and more recently self-navigation (5) have been exploited to compensate for respiratory motion. However, these methods suffer from an inherent operator-dependence, time inefficiency, and complicated workflow.

Recently, a free-running 3D radial data acquisition (6) has been extended with XD-GRASP reconstruction (7) and developed into a fully self-gated free-running framework (8). The free-running framework has been shown to effectively provide anatomical and functional images of the heart with a highly simplified workflow and high sampling efficiency. In order to suppress epicardial fat for improved visualization of the coronary arteries, previous work at 1.5T (6) integrated chemical shift-selective (CHESS) (9) fat saturation modules into a periodically interrupted balanced steady-state free precession (bSSFP) sequence, and linearly increasing RF pulses (ramp-up pulses) were added after each CHESS module to reduce artifacts present in the transient phase of bSSFP (10). The disadvantages of such an approach include an interrupted steady state, a reduced duty cycle, a related time inefficiency, and a high specific absorption rate (SAR) (7).

Lipid-insensitive binomial off-resonant RF excitation (LIBRE) is a recently developed broadband fat suppression technique (11), consisting of two non-selective off-resonant rectangular RF sub-pulses, which has been shown to provide effective fat suppression and insensitivity to main field ($B_0$) and RF field ($B_1$) inhomogeneities. At 3T, LIBRE improved cartilage delineation and the precision of $T_2$ measurements in vivo in human knees (12). Furthermore, LIBRE was shown to attenuate lipid signal and improve vessel detection in ECG-triggered self-navigated T2-prepared

CMRA at 3T as part of a gradient-recalled echo imaging sequence (13). Implemented at 1.5T as part of a balanced steady-state free precession (bSSFP) sequence, LIBRE exhibited robustness to RF field ($B_1$) inhomogeneities in simulations and in vitro, and it effectively suppressed epicardial fat in vivo in ECG-triggered self-navigated T2-prepared CMRA (14). These findings advance the hypothesis that LIBRE could further be integrated into a non-interrupted bSSFP sequence (Figure 1A), as part of the free-running framework, to provide fat-suppressed 5D cardiac images at 1.5T without the need for fat saturation and ramp-up pulses that adversely affect duty cycle, time efficiency, and SAR.

For these reasons, we wanted to implement and optimize LIBRE for non-interrupted free-running bSSFP 5D cardiac MRI at 1.5T, ascertain the magnitude of fat suppression that can be obtained, and test the hypothesis that it achieves quantitative performance comparable to conventional non-interrupted free-running water excitation and to that of the previously-published interrupted free-running approach (6) while reducing scan time and SAR. In pursuit of this goal, we performed numerical simulations and explored the parameter space of LIBRE, including the RF excitation angle, RF frequency, and RF pulse duration, to identify optimal LIBRE parameter settings for bSSFP. Subsequently, we performed in vitro experiments for validation of these simulations. We finally conducted an in vivo study where we quantitatively compared the LIBRE results to those obtained from a free-running bSSFP sequence without fat suppression, as a reference, to those obtained from a free-running bSSFP sequence incorporating a 1-2-1 water excitation, and to those obtained with the previously-published interrupted free-running approach (6). Non-interrupted free-running LIBRE results were also compared to conventional ECG-triggered self-navigated images obtained with fat saturation pre-pulses (15).

## METHODS

### LIBRE background

The LIBRE pulse consists of two rectangular pulses having variable RF frequency ($f_{RF}$), defined relative to the Larmor frequency, sub-pulse duration ($\tau$), and RF excitation angle ($\alpha$) (11). Figure 1A contains a basic schematic of the LIBRE pulse, and additional details can be found in (11). The LIBRE parameters are related by equation (1) (11):

$$\tau = \sqrt{1 - \left(\frac{\alpha}{2\pi}\right)^2} / (\Delta f + \gamma \Delta B_0) \tag{1}$$

where $\Delta f$ is the difference between $f_{RF}$ and the precession frequency of the tissue to be suppressed, $\gamma$ is the gyromagnetic ratio for protons, and $\Delta B_0$ is the local magnetic field inhomogeneity.

### Pulse parameter optimization using Bloch equation simulations

Previously-validated (14) Bloch equation simulations were performed to determine the LIBRE parameter ranges of $f_{RF}$, $\tau$, and $\alpha$ that maximize blood-fat contrast in bSSFP at 1.5T, while ensuring the simulated range for the repetition time (TR) was under 6 ms to minimize the risk of banding artifacts (10) in the heart. The blood-fat contrast was calculated as the difference between blood and fat signal. Blood signal was assumed to be on-resonant, whereas fat signal was modelled using a six-peak fat model as the weighted sum of signals from six chemical off-resonant species (16,17). Identical relaxation times were assumed for each peak, and both off-resonant frequencies and relative amplitudes can be found in Table 1. The range of investigated $\tau$ values was determined by the restriction on TR, as discussed above. $\alpha$ was fixed to a range of 10° to 180°, as SAR limitations effectively prohibit higher RF excitation angles, and the range of $f_{RF}$ values was informed by equation (1), which was used to provide the midpoint of a 400-Hz-wide range for each value of $\tau$. The LIBRE pulse simulations were compared to those from two other non-spatially-selective RF excitation pulses (Figure 1A): first, to a non-fat-suppressing rectangular excitation pulse (SP), to characterize the magnitude of fat suppression obtained with LIBRE; and second, to another water-selective approach that permits a non-interrupted free-running acquisition, namely a spectrally-selective RF-phase-modulated 1-90°-2-90°-1 water excitation (WE) pulse. The independent variable was $\alpha$ for SP and WE. Blood-fat contrast was chosen as the optimization criterion for LIBRE and WE. SP was optimized for blood signal, as it does not

provide inherent fat suppression. Simulation parameters are found in Table 1. The relaxation times (Table 1) used for the simulations were those of the corresponding compartments in the phantom.

Furthermore, the three optimized pulses were assessed for sensitivity to $B_0$ and $B_1$ inhomogeneities by simulating the steady-state transverse magnetization as a function of tissue frequency ($\Delta f_{TISSUE}$), which is the precession frequency relative to the Larmor frequency, and $\alpha$. To measure the effective fat suppression capabilities, the fat suppression band width (FSBW) of each optimized pulse was calculated as the range of fat tissue frequencies encompassing -220 Hz, which corresponds to the dominant peak of the 6-peak fat model above, where the signal was less than 5% of the on-resonant blood signal. The simulated range of $\alpha$ was the same as in Table 1, and the simulated range of $\Delta f_{TISSUE}$ was from -500 to +500 Hz.

**In vitro experiments**

*Data acquisition*

To validate the numerically optimized LIBRE parameter ranges, scans were performed on a phantom containing compartments that mimic the relaxation times of blood, fat, and myocardial tissue. First, the in vitro LIBRE bSSFP signal was examined as a function of α and $f_{RF}$, for $\tau = 1.3$ ms, to ascertain the validity of the numerical simulations. Secondly, the signals of the different compartments obtained with the optimized LIBRE pulse were compared to those of the optimized SP and WE pulses; the scans were repeated six times for statistical analyses. Scans were performed on a 1.5T scanner (MAGNETOM Aera, Siemens Healthcare AG, Erlangen, Germany) with a prototype 3D radial (18) bSSFP sequence, which was identical to the non-ECG-triggered free-breathing non-interrupted free-running bSSFP sequence used for the in vivo scans. The reconstruction of each static phantom image was performed using all radial readouts from all coils. RF excitation pulse and sequence parameter ranges are described in Table 1.

*Data analysis*

The relative RF pulse performance was validated by measuring the signal-to-noise ratio (SNR) in the blood, fat, and myocardium compartments of the phantom, and the contrast-to-noise ratio (CNR) between blood and fat (blood-fat CNR) and blood and myocardium (blood-myocardium CNR). Regions of interest (ROIs) were manually selected in each of the three compartments in

seven consecutive slices in a central region, where the signal appeared homogeneous, using a custom script in MATLAB (The MathWorks, Inc., Natick, MA, USA). The SNR was calculated as the ratio of the mean signal over an ROI containing the tissue of interest and the standard deviation of noise over an ROI drawn outside the phantom. The CNR was calculated as the difference of the SNRs of two tissues.

## In vivo experiments

*Data Acquisition & Imaging Sequences*

In this Institutional Review Board-approved study, whole-heart free-running data were collected at 1.5T (MAGNETOM Aera and MAGNETOM Sola, Siemens Healthcare AG, Erlangen, Germany) using a 32-channel spine coil array and an 18-channel chest coil array. Data were acquired during free-breathing in 21 volunteers (age: $29 \pm 4$ years; 11 male) using a fully self-gated prototype non-interrupted free-running 3D radial bSSFP sequence (8) (Figure 1A) incorporating the LIBRE pulse . In 11 of these volunteers, data were additionally acquired using the same sequence where LIBRE was replaced with SP and WE pulses, and, in 10 other volunteers, data were collected using the previously-published interrupted free-running (IFR) approach (6) (Figure 1B). The order of the acquisitions was randomly permutated among volunteers to avoid fatigue effects. RF pulse specifications and sequence parameters are provided in Table 1. Scan time and specific absorption rate (SAR) as obtained from the "SAR" or "IEC_WHOLE_BODY" field in the DICOM file were recorded for each in vivo scan. In all cases, radial readouts were arranged in interleaves based on a spiral phyllotaxis pattern (18), with successive interleaves rotated about the z-axis by the golden angle. The first readout in each interleave was oriented in the superior-inferior (SI) direction for subsequent physiological motion extraction (8) and binning into cardiac and respiratory phases.

In addition to the above non-triggered free-running acquisitions, a third set of images was acquired using a previously-reported ECG-triggered self-navigated 3D radial sequence (FS) (15) with T2-preparation (19) and CHESS fat saturation modules (isotropic field of view = 220 mm; isotropic voxel size = 1.15 mm; $\alpha = 90°$; TR = 3.3 ms; approximately 12 000 radial readouts; receiver bandwidth = 685 Hz/pixel) in 2 volunteers (age: 26 and 32 years; 1 male) at 1.5T (MAGNETOM Aera, Siemens Healthcare AG, Erlangen, Germany).

*Physiological information extraction and binning*

Physiological motion signal extraction was performed as previously described by Di Sopra et al. 2019 (8) using MATLAB (The MathWorks Inc., Natick, USA). Briefly, SI projections were obtained by applying the 1D Fast Fourier Transform to SI readouts (20), which were sampled every 22 readouts, resulting in an effective temporal resolution of approximately 60 to 120 ms depending on the RF excitation pulse used. Principal component analysis was subsequently performed on these SI projections to extract respiratory signals in a frequency range from 0.1 to 0.7 Hz and cardiac signals in a range from 0.5 to 1.8 Hz. These signals were then used to sort the readouts into non-overlapping cardiac bins with a temporal width of 50 ms, and into four non-overlapping respiratory bins containing equal numbers of readouts, based on the amplitude of the respiratory signal (8).

*Image reconstruction*

The binned k-space data were then reconstructed into motion-resolved images using compressed sensing (21), as described by Feng et al. 2018 (7). Specifically, XD-GRASP (22) solves the following optimization problem while enforcing sparsity along the cardiac and respiratory dimensions:

$$m = arg \min_{m}\|F \cdot C \cdot m - d\|_2^2 + \lambda_c\|D_c m\|_1 + \lambda_r\|D_r m\|_1 \qquad (1)$$

$F$ is the non-uniform FFT, $m$ is the motion-resolved 5D dataset (x, y, z, cardiac, respiratory), $C$ are the coil sensitivities, and $d$ are the sorted k-space data ($k_x$, $k_y$, $k_z$, cardiac, respiratory, coil). $D_c$ and $D_r$ are the first-order difference operators along the cardiac and respiratory dimensions, respectively, and $\lambda_c$ and $\lambda_r$ are the respective regularization weights. Both $\lambda_c$ and $\lambda_r$ were set to 0.01 for all reconstructions to remove variation in regularization weights as an additional confounder; these values were experimentally found to provide a good trade-off between smoothness in the image domain and in the motion temporal domain in a lower-resolution dataset (not shown). No spatial or wavelet regularization was used. The optimization problem in equation (1) was solved using the nonlinear conjugate gradient method with backtracking linesearch (7,23); 36 iterations were used, and the algorithm was restarted every 6 iterations by taking a gradient step to compensate for the loss of conjugacy of successive gradients. Reconstructions were performed using MATLAB on a workstation with two six-core CPUs (Intel Xeon E5, Intel Corporation, Santa

Clara, USA), 512 GB of RAM, and an NVIDIA Tesla K40 GPU (Nvidia Corporation, Santa Clara, USA).

*Data analysis*

The combination of cardiac and respiratory binning resulted in 100 to 120 3D volumes reconstructed for each individual scan. Therefore, one end-expiratory volume corresponding to mid-diastolic quiescence was determined visually and retrospectively selected for subsequent analyses.

In lieu of SNR & CNR analyses, which would not have been feasible due to the noise distribution secondary to the compressed sensing reconstruction, a contrast ratio (CR) analysis was performed for blood-epicardial fat and blood-myocardium. The CR was calculated as the ratio of the mean signals over ROIs drawn in the respective tissues, the first tissue being blood for the case of this analysis. The blood ROI was drawn in the ascending aorta just above the ostium of the RCA, the epicardial fat ROI was drawn in the fat surrounding the RCA, and the myocardium ROI was drawn in the interventricular septum approximately at mid-level between the RCA ostium and the apex. The ROIs were drawn using the Segment Editor extension in 3D Slicer (24) (http://www.slicer.org).

For LIBRE, SP, WE, and IFR, the number of volunteers in whom proximal segments of a minimum length for the following arteries could be visually identified were counted (minimal length given in parentheses): the right coronary artery (RCA, 2 cm), the combined left main and left anterior descending coronary arteries (LM+LAD, 2 cm), and the left circumflex coronary artery (LCX, 1 cm). Vessel length and vessel sharpness, both for the first 4 cm and the entire vessel, of the LIBRE, WE, and IFR datasets were determined using SoapBubble (25); for the LCX, the vessel sharpness for the entire length was computed.

*Statistical analysis*

A Wilcoxon rank sum test, for unpaired data, was used to compare SAR and CR between LIBRE and SP, LIBRE and WE, and LIBRE and IFR; the Bonferroni correction for multiple comparisons was applied. The number of detected arteries between LIBRE and SP (in the subset of 11

volunteers in which both sets of images were acquired), LIBRE and WE (in the subset of 11 volunteers), and LIBRE and IFR (in the subset of 9 volunteers) was compared using NcMemar's test with the Bonferroni correction. Vessel length and vessel sharpness of the RCA, the LM+LAD, and the LCX obtained with LIBRE and WE and LIBRE and IFR were compared using a Wilcoxon rank sum test with the Bonferroni correction. p<0.05 was considered statistically significant and the Bonferroni correction was used where appropriate.

# RESULTS

## Bloch equation simulations

Numerical simulations determined that the LIBRE parameters that optimize blood-fat contrast, while keeping the TR under 6 ms, as recommended by Bieri et al (10), occurred within a range from $\tau = 1.1$ ms to $\tau = 1.5$ ms (Figure 2), from which the midpoint $\tau$ and corresponding $f_{RF}$ and $\alpha$ that maximized blood-fat contrast were taken. Therefore, the optimal parameters were $\tau = 1.3$ ms, $f_{RF} = 540$ Hz, and $\alpha = 120°$ (red dots, Figure 2); the $\alpha$ that maximized blood-fat contrast was $130°$ by a negligible margin, so $120°$ was chosen to reduce SAR. It was found that increasing the sub-pulse duration shifted the regions of high blood signal, high blood-fat contrast, and high blood-myocardium contrast towards lower RF excitation angles (Figure 2; full simulation data not shown) and lower SAR by extension. The myocardium signal did not vary significantly over the investigated LIBRE parameter range (Figure 2).

The results of the numerical simulations for WE and SP are shown in Figure 3, where the corresponding LIBRE simulations (for $\tau = 1.3$ ms and $f_{RF} = 540$ Hz) are also shown for the reader's reference. Optimal RF excitation angles of $40°$ for WE and $50°$ for SP were found (yellow and red dots, respectively, Figure 3). While the fat signal for LIBRE and WE remained low and generally independent of the RF excitation angle (Figure 3B), it was similar to that of blood signal for SP over a relatively broad range of RF excitation angles, as fat signal is not suppressed. This can also be seen in Figure 3D, where the difference in signal response between blood and fat is provided as a function of the RF excitation angle: the blood-fat contrast was positive for LIBRE and WE but fluctuated around zero for SP. When looking at the signal of the myocardium (Figure 3C), it remained relatively low for the entire range of investigated RF excitation angles for all three RF pulses, leading to a high blood-myocardium signal difference for RF excitation angles around $50°$ for SP and WE (Figure 3E), where blood signal was high for both SP and WE, and around $160°$ for LIBRE, whose blood signal plateaued for RF excitation angles above $100°$.

Figure 4 presents the steady-state transverse magnetization of blood for the three numerically-optimized pulses as a function of tissue frequency and RF excitation angle, to enable an assessment of their relative sensitivities to $B_0$ and $B_1$ inhomogeneities. Each pulse exhibited the TR-dependant

signal dropout that leads to banding artifacts in bSSFP images (Figure 4, orange arrows). The white lines indicate the respective numerically-optimized RF excitation angles for each pulse (Figure 4). Examining this signal profile around 0 Hz (water), we see that both LIBRE (Figure 4A) and WE (Figure 4C) possess a slight sensitivity to variations in tissue frequency ($B_0$ inhomogeneities). Following the black line labelled "water" or alternatively Figure 4D, which both show on-resonant signal variation due to changes in the RF excitation angle ($B_1$ inhomogeneities), we see that LIBRE signal exhibited the lowest RF excitation angle-dependence of the three pulses (Figure 4A). Both LIBRE and WE reduced signal around the fat frequency in an RF excitation angle-independent manner, as indicated by the region of reduced signal around the black line labelled "fat" (Figure 4A,C). The calculated FSBW values support this observation: SP had an FSBW of 0 Hz, whereas LIBRE had an FSBW of 21 Hz and WE had an FSBW of 58 Hz. In fact, the reported FSBW corresponds to the range of tissue frequencies along the white line, and centred around -220 Hz, where the signal is less than 5% of the water signal. Although SP does not suppress tissue around -220 Hz, there is a band at approximately -170 Hz (Figure 4B), which might cause signal reductions in fat regions in vivo.

**In vitro experiments**

The results of the LIBRE optimization (Figure 5) and comparison of the optimized LIBRE, SP, and WE pulses (Figure 6) were highly consistent between simulations and in vitro scans. The shapes of corresponding LIBRE signal profiles as functions of α (Figure 5A) and $f_{RF}$ (Figure 5B) are similar between simulations and in vitro scans. In particular, the α and $f_{RF}$ that were predicted by the simulations to maximize LIBRE blood-fat contrast had deviations of 0° and 40 Hz, respectively, with respect to the in vitro scans (Figure 5A,B). The relative signal and contrast of the optimized pulses was generally consistent between simulations and in vitro scans (Figure 6). The only exception was that the fat signal of SP was higher in vitro than that of the simulations and higher than in vitro blood signal, leading to a negative blood-fat contrast that contradicts the near-zero contrast predicted by simulations. Figure 6 indicates that LIBRE was the only pulse to simultaneously provide high blood signal and fat suppression, and had, consequently, the highest blood-fat contrast.

**In vivo experiments**

Fat-suppressed cardiac-and-respiratory-motion-resolved 3D images were successfully reconstructed from in vivo free-running whole-heart data (Supporting Information Video S1 and Supporting Information Video S2), although the acquired data for one volunteer were discarded due to scanner malfunction. Therefore, the sample size was n = 20 for LIBRE and n = 9 for IFR. Reconstruction time ranged from 5 to 8 hours. Respiratory displacement and both cardiac contraction and relaxation of the heart were well-resolved (Supporting Information Video S1 and Supporting Information Video S2). The quantitative results are shown in Table 2. Acquisition times were 11min33s for LIBRE, 11min27s for WE, 6min26s for SP, and 14min06s for IFR (Table 1). They were constant and independent of respiratory patterns and heart rates. The SAR for LIBRE was $0.57 \pm 0.04$ W/kg, which was significantly lower than that of SP ($1.56 \pm 0.14$ W/kg; $p<0.001$), WE ($0.98 \pm 0.09$ W/kg; $p<0.001$), and IFR ($2.43 \pm 0.30$ W/kg, $p<0.001$) (Table 2).

LIBRE provided uniform epicardial fat suppression and improved delineation of coronary arteries relative to SP and WE (Figure 7). With WE, epicardial fat suppression was less consistent (yellow arrows, Figure 7), which, coupled with poor blood signal, led to regionally impaired coronary artery delineation when compared to LIBRE (red arrows, Figure 7). SP was naturally unable to suppress fat (yellow arrows, Figure 7), which often led to an inability to delineate the coronary arteries. However, using SP, some segments of the coronary arteries were visible occasionally, which can be attributed to water-fat signal out-of-phase cancellations in voxels containing both tissues (green arrows, Figure 7).

LIBRE provided more uniform fat suppression and similar blood signal compared to FS and IFR (Figure 8). While LIBRE blood signal is similar to that of IFR in both examples, LIBRE epicardial fat suppression is superior and more consistent (yellow arrows, Figure 8). Moreover, LIBRE reformats do not exhibit the water-fat signal out-of-phase cancellation artifacts that are characteristically seen in IFR reformats (green arrows, Figure 8), although these artifacts are also visible in the very distal part of the LM+LAD of volunteer B with LIBRE. Suppression of subcutaneous fat in the chest wall by LIBRE also appears to be more consistent than that of IFR. Blood signal of FS appears to be slightly superior to that of LIBRE in both cases, although fat

signal appears to be more consistently suppressed with LIBRE, both around the coronary arteries (yellow arrows, Figure 8) as well as in the chest wall.

The contrast ratios of the three approaches are shown in Table 2. LIBRE had the highest blood-fat and blood-myocardium CR, with statistical significance reached for the comparison of blood-fat CR with SP ($p<0.001$) and IFR ($p<0.001$) and for the comparison of blood-myocardium CR with IFR ($p<0.001$).

Detection rates, vessel length, and vessel sharpness of the RCA, LM+LAD, and LCX are also shown in Table 2, where the results of the statistical comparisons between LIBRE and SP, WE, and IFR are also displayed. LIBRE was able to detect the RCA and LM+LAD in 19/20 volunteers and the LCX in 16/20 volunteers, which was higher than those of the other three methods, with statistical significance reached in the comparison with SP for the RCA and LCX. Vessel sharpness values measured in the first 4 cm and for the entire vessel length were highest with LIBRE for all three coronary arteries. LIBRE had the highest vessel length for the RCA, and a vessel length for the LCX that was similar to those of WE and IFR. However, the vessel length of the LM+LAD measured by LIBRE was lower than that of WE but higher than that of IFR.

## DISCUSSION

We successfully incorporated LIBRE RF excitation pulses into a non-interrupted bSSFP sequence to enable fat-suppressed 3D motion-resolved whole-heart coronary MRA at 1.5T using the free-running framework. Numerical optimization of the LIBRE pulse parameters was validated in vitro in phantoms, and informed the parameter ranges for subsequent in vivo scans. Compared to SP, WE, and IFR, LIBRE provided both high blood signal and suppressed fat signal. In vivo, LIBRE scan time was similar to that of WE, approximately twice as long as that of SP, and 18% shorter than that of IFR. LIBRE significantly reduced SAR values compared to SP, WE, and IFR. LIBRE had significantly greater blood-fat CR than SP and the coronary arteries were visible more often. LIBRE improved blood-fat CR and increased the vessel sharpness of all three coronary arteries relative to WE. Compared to the previously-published IFR, LIBRE significantly improved blood-fat CR, had higher detection rates for all three vessels, and maintained vessel length and improved vessel sharpness for the RCA and LM+LAD.

### Water-selective RF excitation pulses in bSSFP

There have been few uses of water-selective RF excitation pulses in non-interrupted bSSFP acquisitions in the literature. Binomial water excitation pulses have been used in bSSFP sequences for musculoskeletal imaging at 1.5T and 3T (26–28). Spectral-spatial RF pulses have been used for abdominal imaging with bSSFP at 3T (29). With regards to cardiac imaging, we were unable to find any studies involving water-selective excitation in non-interrupted bSSFP acquisitions, although Pang et al used binomial 1-2-1 water excitation pulses in a non-interrupted GRE sequence for free-breathing post-contrast 4D CMRA at 3T (30). Therefore, to the best of our knowledge, this study demonstrates the first successful use of a water excitation technique in a non-interrupted bSSFP sequence for a dynamic application.

### Numerical simulations

The simulations performed in this study and that incorporate a 6-peak fat model provide some insights about the LIBRE pulse. The results help contextualize a previous study that used a shorter LIBRE sub-pulse duration of 0.7 ms where it was concluded that blood signal remained to be optimized (14). In fact, increasing the sub-pulse duration reduced the off-resonant RF frequency

required for effective fat suppression, which was also found in (11), with the benefit that on-resonant blood and myocardium signals were increased (Figure 2). This observation guided the choice of LIBRE parameters used in this study. Coincidentally, increasing the sub-pulse duration, and thus the total pulse duration, reduced SAR values at the expense of a slight increase in TR. Compared to SP, LIBRE and WE have a TR that is almost twice as long (Table 1), implying that there is a time cost for fat suppression. Naturally, the increase in TR comes at an increased risk of banding artifacts localized in the region of the heart. Furthermore, although the fat signal, and, consequently, blood-fat contrast, appears to be sensitive to variations in the RF excitation frequency (Figure 2), the practical likelihood of variations in RF frequency is low, as RF synthesizers can generally generate waveforms with the desired frequency with very high accuracy.

The in vitro and in vivo findings point to the merits of numerical optimization using Bloch equation simulations and the 6-peak fat model. The Bloch equation simulations used in this study have been validated previously (14) and are able to model relevant theoretical bSSFP signal characteristics described in the literature (10). Simulations predicted that LIBRE would have the highest blood-fat contrast, which was confirmed in vitro (Figure 6) and produced in vivo images with the highest vessel sharpness and highest blood-fat contrast ratio (Table 2). There were cases where the simulations did not perfectly match the in vitro or in vivo behaviour. The in vitro fat signal of SP was higher than theoretically predicted (Figure 6), and there were slight discrepancies between simulated LIBRE signal behaviour and that in vitro (Figure 5). In both cases, the fact that each tissue was modelled with only a single $T_1$ and $T_2$, and a limited number of off-resonance values (reflecting $B_0$ inhomogeneities), could have contributed to such minor differences. With regards to the high in vitro SP fat signal, it is possible that higher proton density in the fat compartment of the phantom could have caused such high signal, which the simulations, assuming constant proton densities, would not have been able to predict without further information. Furthermore, the lower FSBW of LIBRE compared to WE did not appear to be reflected in the vessel sharpness values, but might explain the lower vessel lengths of the LM+LAD and LCX in LIBRE images compared to WE images. Numerical simulations suggested that LIBRE had higher blood-fat contrast, which may explain the higher vessel sharpness values, but it had a lower FSBW than WE, meaning that fat suppression would have been less consistent in areas further away from the isocentre and the

heart, where vessel diameter gradually decreases due to branching and $B_0$ inhomogeneities become more severe, potentially affecting the discernible vessel length. Nevertheless, numerical simulations with even simple models, such as those used here, can guide in vivo parameter settings by predicting optimal pulse parameters and characterizing signal.

One potential drawback of the present numerical simulations is that the relaxation times were those of the phantom, rather than in vivo values. Retrospectively, we performed numerical simulations using the same six-peak fat model as before but with relaxation times for blood (31), fat (32), and myocardium (33,34) that were measured in vivo. The results for the numerical optimization of LIBRE are presented in Supporting Information Figure S1, and the results of the numerical optimization of SP and WE are presented in Supporting Information Figure S2. The optimal parameters for SP and WE (Figure S2) did not change compared to the current simulations (Figure 3), although, for $\tau = 1.3$ ms, the optimal LIBRE parameters were $\alpha = 140°$ and $f_{RF} = 540$ Hz (Figure S1), which represents a 20° change for $\alpha$. These results indicate that the behaviour of these three pulses is relatively insensitive to the choice of relaxation times, and that the present simulations were sufficiently accurate for modelling pulse behaviour in vitro and in vivo.

Finally, the fat model used here provides insights into pulse optimization for CMRA. The three main peaks of the present fat model, at -166 Hz, -217 Hz, and -243 Hz (Table 1), all fall within the region of tissue frequencies suppressed by LIBRE and WE (Figure 4). Furthermore, an in vivo myocardial triglyceride spectroscopy study noted that epicardial lipids exhibited a peak at -3.1 ppm that was not detected in myocardial lipids (35), which would correspond to -198 Hz at 1.5T. The fact that both LIBRE and WE suppressed signal at all four of these resonant frequencies (Figure 4) could explain why they were generally able to suppress epicardial fat in vivo for CMRA, and provides guidance for future studies as to the range of fat frequencies that need to be suppressed for successful CMRA. Furthermore, to account for in vivo variation in lipid composition, future studies should ensure that a range of fat frequencies, centred around -3.1 ppm and -3.4 ppm, are suppressed.

**3D whole-heart CMRA approaches**

This study included a comparison with a previously-reported free-running bSSFP sequence that is periodically interrupted for fat suppression (IFR) (6). LIBRE scan time was reduced by 18% when compared to IFR (Table 1). While LIBRE affords the advantage of removing the fat saturation and ramp-up pre-pulses, the TR is inherently increased, and therefore the gain in scanning time is modest. However, SAR was reduced by 77% relative to IFR (Table 2). LIBRE provides more consistent fat signal suppression both around the RCA and LM+LAD as much as in the anterior chest when compared to IFR (Figure 8). Moreover, LIBRE provides vessel delineation through blood-fat contrast alone, whereas vessel delineation in IFR images appears to have been largely due to and artificially overemphasized by the presence of water-fat phase cancellation artifacts, as the mean blood-fat CR of 1.2 indicated little difference between blood and epicardial fat signal in IFR images. These artifacts, which were frequently seen in the present IFR images (full data not shown) and also retrospectively in images in (6,7), generate sharp vessel edges that artificially increase vessel sharpness values, and likely account for the similarity in vessel sharpness values between LIBRE and IFR data despite the qualitatively superior fat suppression observed in the LIBRE images.

With regards to the comparison with the ECG-triggered self-navigated FS method, the free-running LIBRE approach has several advantages. Preliminary examination in two volunteers suggests that LIBRE provides more consistent fat suppression, while FS provides slightly higher blood signal. The higher blood signal may be due to the ECG triggering, as the trigger delay would allow for magnetization recovery. A more comprehensive quantitative study would be necessary for concrete conclusions. On a more general level, the LIBRE approach uses all readouts, thereby increasing sampling efficiency, and providing motion-resolved 5D images rather than respiratory-motion-corrected 3D images. The free-running LIBRE approach also greatly reduces operator-dependence relative to FS, because the need for the ECG set-up is eliminated.

Finally, although we did not compare our non-interrupted free-running LIBRE approach with conventional ECG-triggered (36), navigator-gated (37,38), fat-saturated, T2-prepared (19,39) 3D Cartesian CMRA, we will proceed with a brief discussion of the two approaches. The conventional approach provides motion-corrected images through the use of ECG triggering in mid-diastole for

cardiac motion compensation and the use of respiratory navigators for respiratory motion correction, with T2-preparation used to improve blood-myocardium contrast and fat saturation to improve blood-fat contrast. Conversely, our free-running non-interrupted LIBRE bSSFP approach provides cardiac- and respiratory-motion-resolved images without the need for ECG or navigators, with blood-myocardium contrast intrinsically provided by bSSFP (2) and fat signal attenuation through LIBRE. The benefits of our approach are that it provides isotropic motion-resolved 3D images with a simplified workflow – eliminating the need to apply the ECG and position the navigator – while scanning time is constant and independent of heart rate or respiratory patterns. The sampling efficiency is high at around 30%, as all the data, whose acquisition accounts for approximately 30% of the scan duration, are used to reconstruct the 5D images. Conversely, the conventional ECG-triggered and navigator-gated approach suffers from a significantly reduced sampling efficiency of 2% only, as data used for image reconstruction are only collected when both favorable cardiac and respiratory phases coincide. In addition, the acquisition time of the conventional approach can be unpredictable and vary due to many factors, including the low acceptance rate of the respiratory gating (15), positioning of the navigator (40), and changes in the respiratory (41) or cardiac cycle (6) during the scan. However, like FS, the conventional approach potentially benefits from higher SNR as the ECG trigger delay allows for magnetization recovery. Furthermore, the use of T2-preparation provides increased blood-myocardium contrast, but this increase may be offset to a certain degree by the intrinsic blood-myocardium contrast of bSSFP (2).

**Study limitations**

The study methodology contained some shortcomings. The LIBRE pulse was compared to a 1-2-1 water excitation pulse that was available on the scanner, and, apart from an RF excitation angle optimization, no further optimization of this pulse was performed. Recent work has demonstrated that fast interrupted steady-state (FISS) (42) can be exploited for fat-saturated 5D free-running cardiac imaging (43,44), and a comparison with the present approach would be very instructive. The reconstruction pipeline, including regularization weights, was identical for LIBRE, SP, WE, and IFR, although optimal regularization weights are expected to vary as each acquisition will have slightly different noise levels and residual aliasing. The identification of the mid-diastolic phase was done visually and separately for each dataset, without consideration of coronary artery

vessel length or sharpness. Therefore, coronary artery visualization for these data could potentially be further improved through the use of pulse-specific regularization weights and a more quantitative approach for extracting the mid-diastolic resting phase.

Furthermore, this study did not measure cardiac function. However,  LIBRE acquisitions can potentially provide cardiac functional information, since previous studies involving free-breathing 3D radial bSSFP or GRE acquisitions, with (7) and without (6,30)  compressed sensing reconstructions, showed good agreement with 2D cine acquisitions in terms of left ventricular end-systolic volumes, end-diastolic volumes, and ejection fraction.

## CONCLUSIONS

The LIBRE pulse was numerically optimized and successfully used for fat-suppressed fully self-gated non-interrupted free-running 5D bSSFP cardiac MRI at 1.5T. In vivo, LIBRE improved blood-fat contrast and vessel sharpness and maintained vessel length relative to non-interrupted free-running WE and the previously-published interrupted free-running IFR, while reducing scan time and SAR relative to IFR. LIBRE could potentially offer motion-resolved coronary MRA and functional imaging of the heart at high spatial resolution, with a simplified workflow compared to more conventional cardiac MRI protocols.

# REFERENCES

1. Benjamin EJ, Muntner P, Alonso A, et al. Heart Disease and Stroke Statistics—2019 Update: A Report From the American Heart Association. *Circulation*. 2019;135(10):e146-e603. doi:10.1161/CIR.0000000000000659.

2. Stuber M, Weiss RG. Coronary magnetic resonance angiography. *J Magn Reson Imaging*. 2007;26(2):219-234. doi:10.1002/jmri.20949.

3. Dweck MR, Puntmann VO, Vesey AT, Fayad ZA, Nagel E. MR Imaging of Coronary Arteries and Plaques. *JACC Cardiovasc Imaging*. 2016;9(3):306-316. doi:10.1016/j.jcmg.2015.12.003.

4. Sakuma H, Ichikawa Y, Chino S, Hirano T, Makino K, Takeda K. Detection of Coronary Artery Stenosis With Whole-Heart Coronary Magnetic Resonance Angiography. *J Am Coll Cardiol*. 2006;48(10):1946-1950. doi:10.1016/j.jacc.2006.07.055.

5. Piccini D, Monney P, Sierro C, et al. Respiratory Self-navigated Postcontrast Whole-Heart Coronary MR Angiography: Initial Experience in Patients. *Radiology*. 2014;270(2):378-386. doi:10.1148/radiol.13132045.

6. Coppo S, Piccini D, Bonanno G, et al. Free-running 4D whole-heart self-navigated golden angle MRI: Initial results. *Magn Reson Med*. 2015;74(5):1306-1316. doi:10.1002/mrm.25523.

7. Feng L, Coppo S, Piccini D, et al. 5D whole-heart sparse MRI. *Magn Reson Med*. 2018;79(2):826-838. doi:10.1002/mrm.26745.

8. Di Sopra L, Piccini D, Coppo S, Stuber M, Yerly J. An automated approach to fully self-gated free-running cardiac and respiratory motion-resolved 5D whole-heart MRI. *Magn Reson Med*. 2019;82(6):2118-2132. doi:10.1002/mrm.27898.

9. Haase A, Frahm J, Hanicke W, Matthaei D. 1H NMR chemical shift selective (CHESS) imaging. *Phys Med Biol*. 1985;30(4):341-344. doi:10.1088/0031-9155/30/4/008.

10. Bieri O, Scheffler K. Fundamentals of balanced steady state free precession MRI. *J Magn Reson Imaging*. 2013;38(1):2-11. doi:10.1002/jmri.24163.

11. Bastiaansen JAM, Stuber M. Flexible water excitation for fat-free MRI at 3T using lipid insensitive binomial off-resonant RF excitation (LIBRE) pulses. *Magn Reson Med*.

2018;79(6):3007-3017. doi:10.1002/mrm.26965.

12. Colotti R, Omoumi P, van Heeswijk RB, Bastiaansen JAM. Simultaneous fat-free isotropic 3D anatomical imaging and T2mapping of knee cartilage with lipid-insensitive binomial off-resonant RF excitation (LIBRE) pulses. *J Magn Reson Imaging*. 2018:1-10. doi:10.1002/jmri.26322.

13. Bastiaansen JAM, van Heeswijk RB, Stuber M, Piccini D. Noncontrast free-breathing respiratory self-navigated coronary artery cardiovascular magnetic resonance angiography at 3 T using lipid insensitive binomial off-resonant excitation (LIBRE). *J Cardiovasc Magn Reson*. 2019;21(1):38. doi:10.1186/s12968-019-0543-6.

14. Masala N, Bastiaansen JAM, Piccini D, Stuber M. Fat suppression in 3D bSSFP coronary MRA using lipid-insensitive binomial off-resonant RF excitation (LIBRE) pulses. In: *Proceedings of the Society for Cardiovascular Magnetic Resonance 22nd Annual Scientific Sessions*. Bellevue, USA; 2019.

15. Piccini D, Littmann A, Nielles-Vallespin S, Zenge MO. Respiratory self-navigation for whole-heart bright-blood coronary MRI: Methods for robust isolation and automatic segmentation of the blood pool. *Magn Reson Med*. 2012;68(2):571-579. doi:10.1002/mrm.23247.

16. Hamilton G, Yokoo T, Bydder M, et al. In vivo characterization of the liver fat 1H MR spectrum. *NMR Biomed*. 2011;24(7):784-790. doi:10.1002/nbm.1622.

17. Wang X, Hernando D, Reeder SB. Sensitivity of chemical shift-encoded fat quantification to calibration of fat MR spectrum. *Magn Reson Med*. 2016;75(2):845-851. doi:10.1002/mrm.25681.

18. Piccini D, Littmann A, Nielles-Vallespin S, Zenge MO. Spiral phyllotaxis: The natural way to construct a 3D radial trajectory in MRI. *Magn Reson Med*. 2011;66(4):1049-1056. doi:10.1002/mrm.22898.

19. Brittain JH, Hu BS, Wright GA, Meyer CH, Macovski A, Nishimura DG. Coronary Angiography with Magnetization-Prepared T2 Contrast. *Magn Reson Med*. 1995;33:689-696.

20. Stehning C, Börnert P, Nehrke K, Eggers H, Stuber M. Free-breathing whole-heart coronary MRA with 3D radial SSFP and self-navigated image reconstruction. *Magn Reson Med*. 2005;54(2):476-480. doi:10.1002/mrm.20557.

21. Donoho DL. Compressed Sensing. *IEEE Trans Inf Theory*. 2006;52(4):1289-1306. doi:10.1109/TIT.2006.871582.

22. Feng L, Axel L, Chandarana H, Block KT, Sodickson DK, Otazo R. XD-GRASP: Golden-angle radial MRI with reconstruction of extra motion-state dimensions using compressed sensing. *Magn Reson Med*. 2016;75(2):775-788. doi:10.1002/mrm.25665.

23. Lustig M, Donoho D, Pauly JM. Sparse MRI: The application of compressed sensing for rapid MR imaging. *Magn Reson Med*. 2007;58(6):1182-1195. doi:10.1002/mrm.21391.

24. Fedorov A, Beichel R, Kalpathy-Cramer J, et al. 3D Slicer as an image computing platform for the Quantitative Imaging Network. *Magn Reson Imaging*. 2012;30(9):1323-1341. doi:10.1016/j.mri.2012.05.001.

25. Etienne A, Botnar RM, Van Muiswinkel AMC, Boesiger P, Manning WJ, Stuber M. "Soap-Bubble" visualization and quantitative analysis of 3D coronary magnetic resonance angiograms. *Magn Reson Med*. 2002;48(4):658-666. doi:10.1002/mrm.10253.

26. Kornaat PR, Doornbos J, van der Molen AJ, et al. Magnetic resonance imaging of knee cartilage using a water selective balanced steady-state free precession sequence. *J Magn Reson Imaging*. 2004;20(5):850-856. doi:10.1002/jmri.20194.

27. Duc SR, Koch P, Schmid MR, Horger W, Hodler J, Pfirrmann CWA. Diagnosis of Articular Cartilage Abnormalities of the Knee: Prospective Clinical Evaluation of a 3D Water-Excitation True FISP Sequence. *Radiology*. 2007;243(2):475-482. doi:10.1148/radiol.2432060274.

28. Ribot EJ, Wecker D, Trotier AJ, et al. Water Selective Imaging and bSSFP Banding Artifact Correction in Humans and Small Animals at 3T and 7T, Respectively. Zhang H, ed. *PLoS One*. 2015;10(10):e0139249. doi:10.1371/journal.pone.0139249.

29. Yuan J, Madore B, Panych LP. Fat–water selective excitation in balanced steady-state free precession using short spatial–spectral RF pulses. *J Magn Reson*. 2011;208(2):219-224. doi:10.1016/j.jmr.2010.11.005.

30. Pang J, Sharif B, Fan Z, et al. ECG and navigator-free four-dimensional whole-heart coronary MRA for simultaneous visualization of cardiac anatomy and function. *Magn Reson Med*. 2014;72(5):1208-1217. doi:10.1002/mrm.25450.

31. Stanisz GJ, Odrobina EE, Pun J, et al. T1, T2 relaxation and magnetization transfer in tissue at 3T. *Magn Reson Med*. 2005;54(3):507-512. doi:10.1002/mrm.20605.

32. de Bazelaire CMJ, Duhamel GD, Rofsky NM, Alsop DC. MR Imaging Relaxation Times of Abdominal and Pelvic Tissues Measured in Vivo at 3.0 T: Preliminary Results. *Radiology*. 2004;230(3):652-659. doi:10.1148/radiol.2303021331.

33. Chow K, Flewitt JA, Green JD, Pagano JJ, Friedrich MG, Thompson RB. Saturation recovery single-shot acquisition (SASHA) for myocardial T 1 mapping. *Magn Reson Med*. 2014;71(6):2082-2095. doi:10.1002/mrm.24878.

34. Sprinkart AM, Luetkens JA, Träber F, et al. Gradient Spin Echo (GraSE) imaging for fast myocardial T2 mapping. *J Cardiovasc Magn Reson*. 2015;17(1):12. doi:10.1186/s12968-015-0127-z.

35. Szczepaniak LS, Dobbins RL, Metzger GJ, et al. Myocardial triglycerides and systolic function in humans: In vivo evaluation by localized proton spectroscopy and cardiac imaging. *Magn Reson Med*. 2003;49(3):417-423. doi:10.1002/mrm.10372.

36. Edelman RR, Manning WJ, Burstein D, Paulin S. Coronary arteries: Breath-hold MR angiography. *Radiology*. 1991;181(3):641-643. doi:10.1148/radiology.181.3.1947074.

37. Ehman RL, Felmlee JP. Adaptive technique for high-definition MR imaging of moving structures. *Radiology*. 1989;173(1):255-263. doi:10.1148/radiology.173.1.2781017.

38. Li D, Kaushikkar S, Haacke EM, et al. Coronary Arteries: Three-dimensional MR Imaging with Retrospective Respiratory Gating. *Radiology*. 1996;201:857-863.

39. Botnar RM, Stuber M, Danias PG, Kissinger K V., Manning WJ. Improved Coronary Artery Definition With T2-Weighted, Free-Breathing, Three-Dimensional Coronary MRA. *Circulation*. 1999;99(24):3139-3148. doi:10.1161/01.CIR.99.24.3139.

40. Stuber M, Botnar RM, Danias PG, Kissinger K V., Manning WJ. Submillimeter Three-dimensional Coronary MR Angiography with Real-time Navigator Correction: Comparison of Navigator Locations. *Radiology*. 1999;212(2):579-587. doi:10.1148/radiology.212.2.r99au50579.

41. Taylor AM, Jhooti P, Firmin DN, Pennell DJ. Automated monitoring of diaphragm end-expiratory position for real-time navigator echo MR coronary angiography. *J Magn Reson Imaging*. 1999;9(3):395-401. doi:10.1002/(SICI)1522-2586(199903)9:3<395::AID-JMRI6>3.0.CO;2-Y.

42. Koktzoglou I, Edelman RR. Radial fast interrupted steady-state (FISS) magnetic resonance imaging. *Magn Reson Med*. 2018;79(4):2077-2086. doi:10.1002/mrm.26881.

43. Küstner T, Bustin A, Jaubert O, Neji R, Prieto C, Botnar R. 3D Cartesian fast interrupted steady-state (FISS) imaging. *Magn Reson Med*. 2019;82(5):1617-1630. doi:10.1002/mrm.27830.

44. Bastiaansen JAM, Piccini D, Di Sopra L, et al. Natively fat-suppressed 5D whole-heart MRI with a radial free-running fast-interrupted steady-state (FISS) sequence at 1.5T and 3T. *Magn Reson Med*. 2020;83(1):45-55. doi:10.1002/mrm.27942.

**List of Tables**

Table 1. RF excitation pulse and sequence parameters for numerical simulations and in vitro and in vivo experiments.

| | Simulations | In vitro | In vivo |
|---|---|---|---|
| **LIBRE** | | | |
| $\alpha$ [°] | 10 to 180 | 10 to 180 | 120 |
| $\tau$ [ms] | 0.5 to 1.5 | 1.3 | 1.3 |
| Total excitation duration [ms] | 1.0 to 3.0 | 2.6 | 2.6 |
| $f_{RF}$ [Hz] | 220 to 1900 | 320 to 720 | 500 |
| TE / TR [ms/ms] | 1.88 / 3.76 to 2.88 / 5.76 | 2.69 / 5.36 | 2.75 / 5.48 |
| Acquisition time [min:s] | | 00:39 | 11:33 |
| | | | |
| **SP** | | | |
| $\alpha$ [°] | 10 to 180 | 50 | 50 |
| $\tau$ [ms] | 0.3 | 0.3 | 0.3 |
| TE / TR [ms/ms] | 1.47 / 2.93 | 1.47 / 2.93 | 1.53 / 3.05 |
| Acquisition time [min:s] | | 00:21 | 6:26 |
| | | | |
| **WE** | | | |
| $\alpha$ [°] | 10 to 60 | 40 | 40 |
| $\tau$ [ms] | 0.3 | 0.3 | 0.3 |
| Total excitation duration [ms] | 2.68 | 2.68 | 2.68 |
| TE / TR [ms/ms] | 2.66 / 5.31 | 2.66 / 5.31 | 2.72 / 5.43 |
| Acquisition time [min:s] | | 00:39 | 11:27 |
| | | | |
| **IFR** | | | |
| $\alpha$ [°] | | | 90 |
| $\tau$ [ms] | | | 0.3 |
| TE / TR [ms/ms] | | | 1.53 / 3.05 |
| Acquisition time [min:s] | | | 14:06 |
| | | | |
| **Sequence** | | | |
| FOV [mm x mm x mm] | | 180 x 180 x 180 | 220 x 220 x 220 |
| Iso voxel size [mm] | | 1.25 | 1.15 |
| Receiver BW [Hz/pixel] | | 1021 | 1042 |
| # radial readouts | | 7260 | 126478 |
| | | | |
| **Simulation parameters** | | | |
| Blood $T_1$ / $T_2$ [ms/ms] | 1439 / 244 | | |
| Fat $T_1$ / $T_2$ [ms/ms] | 154 / 44 | | |

| | |
|---|---|
| Fat sub-species resonant frequency [Hz] (relative amplitude [%]) | 38 (4.7), -32 (3.9), -125 (0.6), -166 (12), -217 (70), -243 (8.8) |
| Myocardium $T_1$ / $T_2$ [ms/ms] | 989 / 33 |
| Step size [μs] | 1 |

Abbreviations: α: RF excitation angle; $f_{RF}$: RF excitation frequency; τ: sub-pulse duration; TE: echo time; TR: repetition time; min: minutes; FOV: field of view; Iso voxel size: isotropic voxel size; Receiver BW: receiver bandwidth; $T_1$: longitudinal relaxation time; $T_2$: transverse relaxation time

Table 2. Summary of in vivo results. Data are presented as mean ± standard deviation, except for the coronary artery detection rates. Asterisks (*) indicate statistically significant differences in the comparison with LIBRE data. For the vessel sharpness analysis (vessel length, % VS first 4 cm, % VS), no comparison between LIBRE and SP data was performed, as mentioned in the Methods.

| | LIBRE | SP | WE | IFR |
|---|---|---|---|---|
| **SAR** [W/kg] | $0.57 \pm 0.04$ | $1.56 \pm 0.14$* | $0.98 \pm 0.09$* | $2.43 \pm 0.30$* |
| **Contrast ratio** | | | | |
| Blood – fat | $3.9 \pm 1.8$ | $1.1 \pm 0.5$* | $2.7 \pm 1.3$ | $1.2 \pm 0.7$* |
| Blood – myocardium | $1.7 \pm 0.5$ | $1.5 \pm 0.2$ | $1.6 \pm 0.4$ | $1.1 \pm 0.1$* |
| **RCA** | | | | |
| Detection rate | 19/20 | 3/11* | 10/11 | 6/9 |
| Vessel length [cm] | $9.7 \pm 4.0$ | | $8.0 \pm 4.0$ | $9.6 \pm 5.3$ |
| % VS first 4 cm | $54.5 \pm 10.6$ | | $46.5 \pm 12.7$ | $45.3 \pm 10.1$ |
| % VS | $47.1 \pm 10.2$ | | $44.6 \pm 13.2$ | $40.8 \pm 6.9$ |
| **LM+LAD** | | | | |
| Detection rate | 19/20 | 3/11 | 10/11 | 4/9 |
| Vessel length [cm] | $7.4 \pm 2.8$ | | $8.1 \pm 1.8$ | $6.4 \pm 1.8$ |
| % VS first 4 cm | $48.6 \pm 12.5$ | | $47.5 \pm 10.2$ | $39.4 \pm 3.8$ |
| % VS | $51.5 \pm 10.2$ | | $50.7 \pm 10.2$ | $42.1 \pm 6.8$ |
| **LCX** | | | | |
| Detection rate | 16/20 | 3/11* | 8/11 | 1/9 |
| Vessel length [cm] | $2.8 \pm 1.0$ | | $2.9 \pm 1.1$ | 3.1 |
| % VS | $42.4 \pm 7.0$ | | $39.9 \pm 6.0$ | 42.1 |

Abbreviations: SAR: specific absorption rate; RCA: right coronary artery; LM: left main coronary artery; LAD: left anterior descending coronary artery; LX: left circumflex coronary artery; min: minutes.

**List of Figure Captions and Supplementary Material**

Figure 1. Schematic of the A) non-interrupted and B) interrupted free-running bSSFP sequences (not to temporal scale), with model cardiac and respiratory cycles. Each green box is symbolic of one repetition time: an RF excitation pulse followed by a radial readout in k-space. $f_{RF}$: RF frequency; $\tau$: (sub)pulse duration.
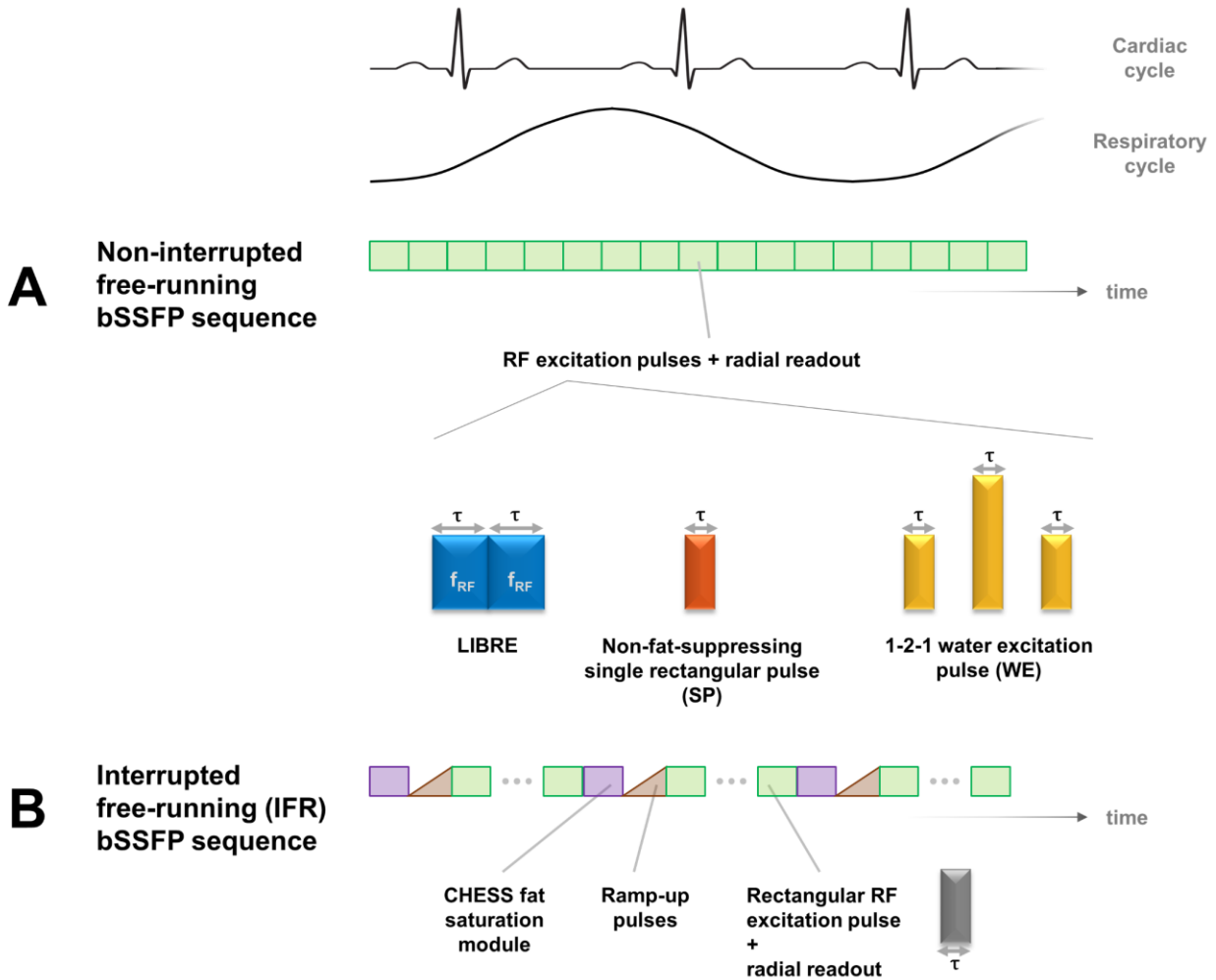
Figure 2: Theoretical LIBRE signal behavior. Transverse steady-state magnetization ($M_{ss}$), as a function of RF excitation angle and frequency (relative to the Larmor frequency) for different sub-pulse durations ($\tau$) of the LIBRE pulse, for blood, fat (6-peak model), myocardium, blood-fat contrast, and blood-myocardium contrast. The red dot indicates the chosen optimal parameters, which maximize the blood-fat contrast.
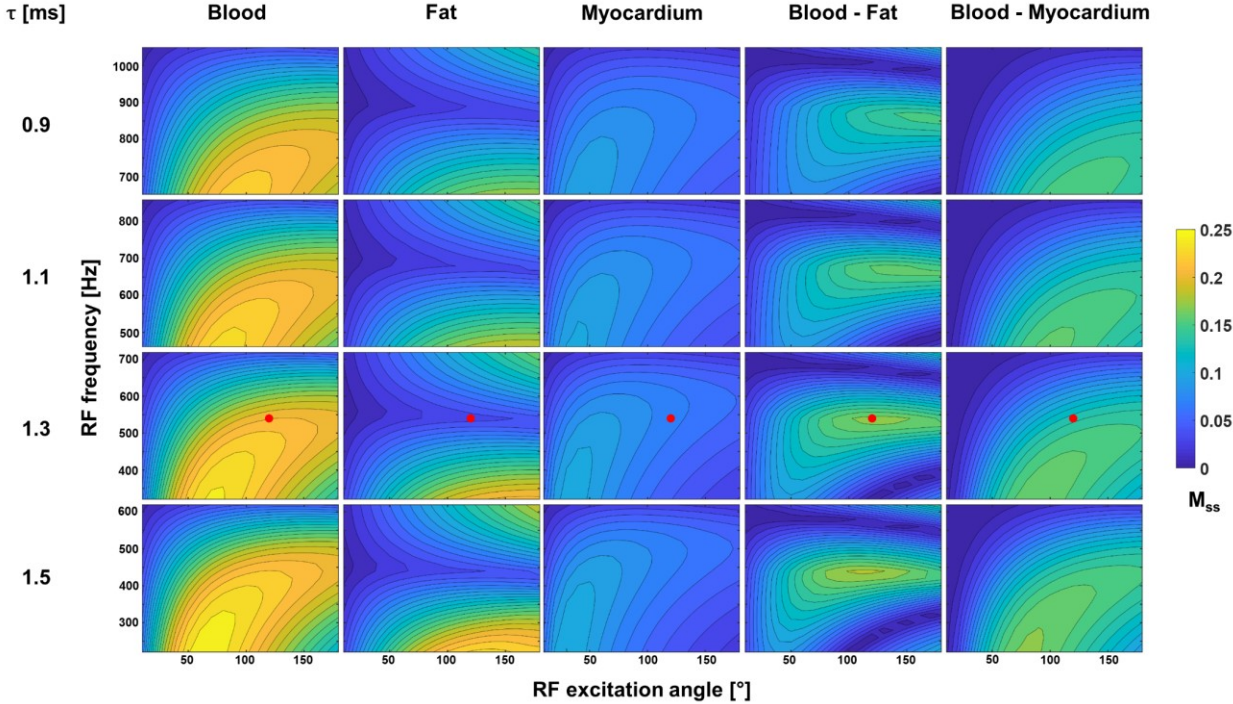
Figure 3: Theoretical LIBRE ($\tau$ = 1.3 ms, $f_{RF}$ = 540 Hz), SP, and WE signal behaviour. Transverse steady-state magnetization ($M_{ss}$) as a function of RF excitation angle for A) blood, B) fat (6-peak model), C) myocardium, D) blood-fat contrast, and E) blood-myocardium contrast. The blue and yellow dots indicate the LIBRE and WE parameters, respectively, that optimize blood-fat contrast, and the red dot indicates the SP parameters that optimize blood signal.
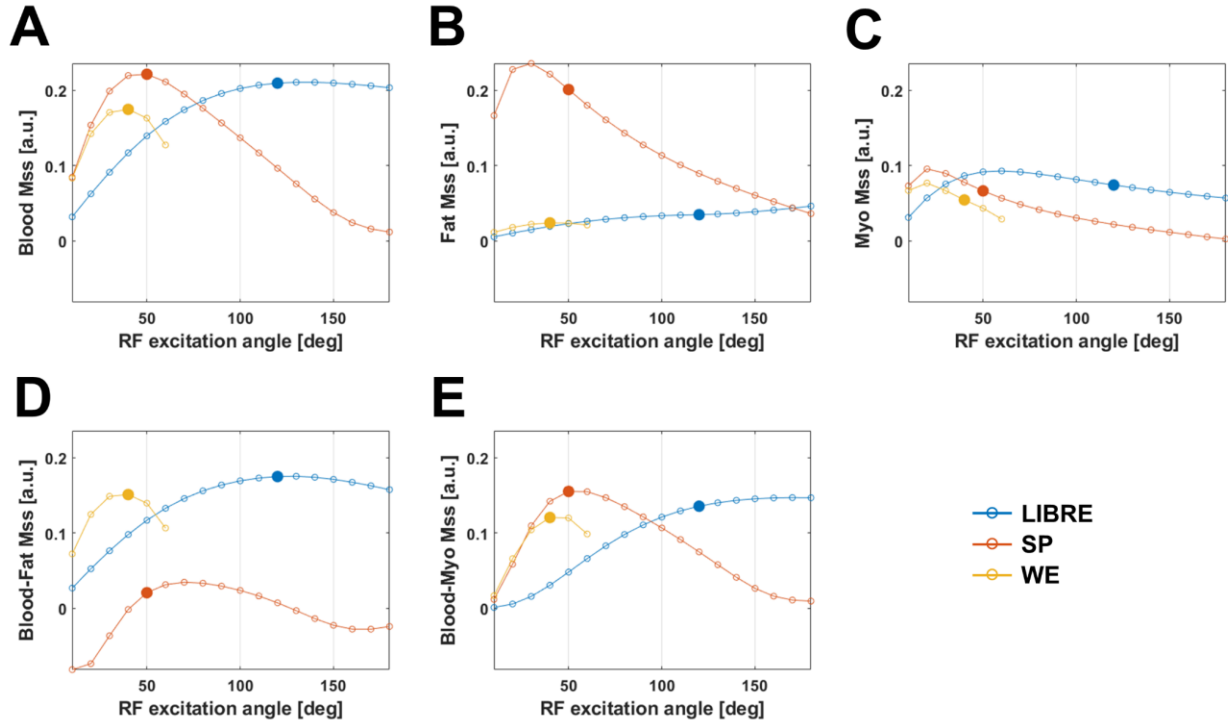
Figure 4: Effect of $B_0$ and $B_1$ inhomogeneities. Transverse steady-state magnetization ($M_{ss}$) as a function of tissue frequency and RF excitation angle for blood tissue, for the A) LIBRE, B) SP, and C) WE RF excitation pulses. D) Transverse steady-state magnetization ($M_{ss}$) as a function of RF excitation angle for on-resonant blood tissue for LIBRE, SP, and WE. In A), B), and C), water (0 Hz) and fat (-220 Hz) resonant frequencies are indicated with dashed black lines; the orange arrows indicate banding artifacts; and the numerically-optimized RF excitation angle for each pulse is indicated by the white dashed lines. Pulse parameters are those found under "In vitro" in Table 1; specifically, for LIBRE, the RF frequency ($f_{RF}$ = 540 Hz) and sub-pulse duration ($\tau$ = 1.3 ms) used the numerically-optimized values.
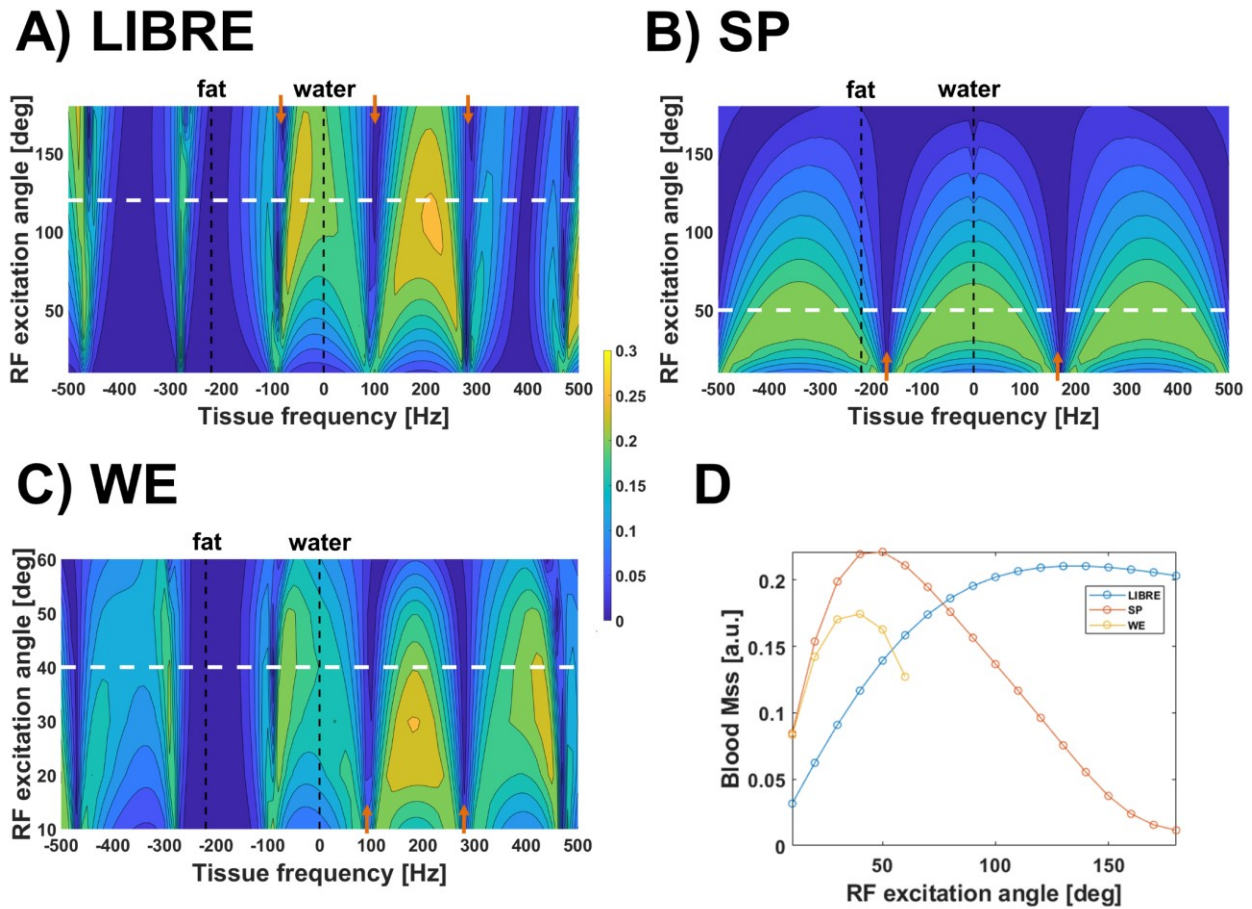
Figure 5: Comparison of simulated (transverse steady-state magnetization; solid line) and in vitro (dashed line) LIBRE bSSFP signal. Blood, fat, and myocardium signal, and blood-fat and blood-myocardium contrast, are shown as a function of A) RF excitation angle and B) RF frequency (relative to the Larmor frequency). The simulation scale is on the left side of the plots and the in vitro SNR scale is on the right side.
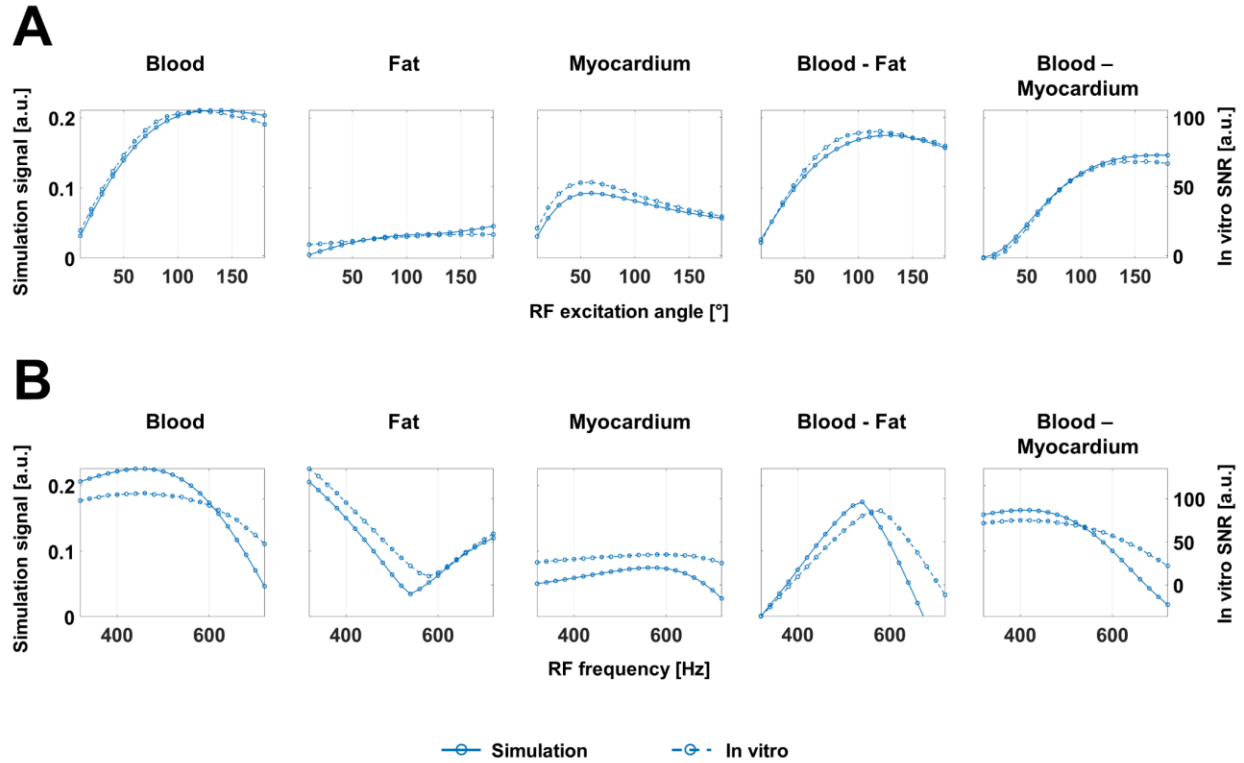
Figure 6: Comparison of simulated (transverse steady-state magnetization) and in vitro bSSFP signal. Blood, fat, and myocardium (myo) signal, and blood-fat and blood-myocardium contrast, are displayed for LIBRE, SP, and WE. Solid bars indicate simulation values and bars with white dashed lines indicate in vitro values. The mean value of the six in vitro repetitions is indicated by the bar height, and the standard deviation is indicated by the error bars. The data have been normalized to the blood signal of LIBRE for both cases: 0.2093 for the simulation data and 85.90 for the in vitro data.
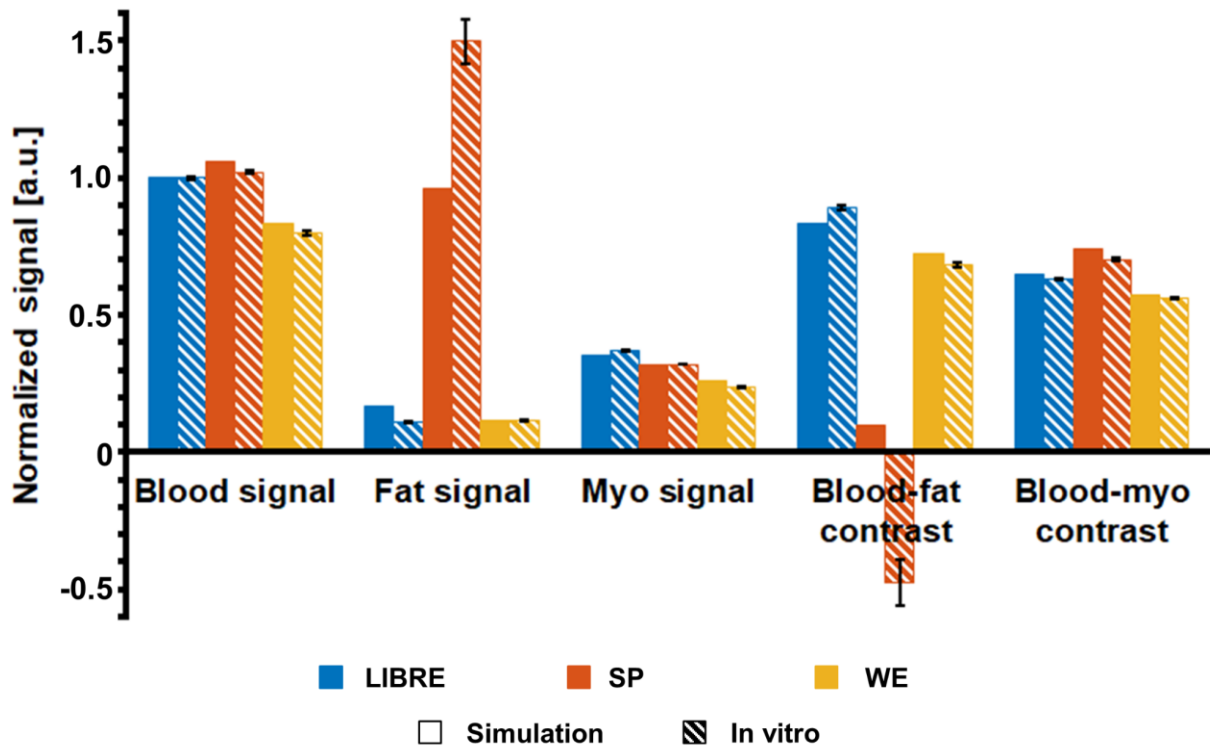
Figure 7: Free-running reformatted images of the right coronary artery (RCA), left main and left anterior descending artery (LM+LAD), and left circumflex artery (LCX), obtained with LIBRE, SP, and WE RF excitation pulses. Yellow arrows indicate regions of epicardial fat, red arrows indicate (expected) coronary artery edges, and green arrows show water-fat phase cancellation artifacts.
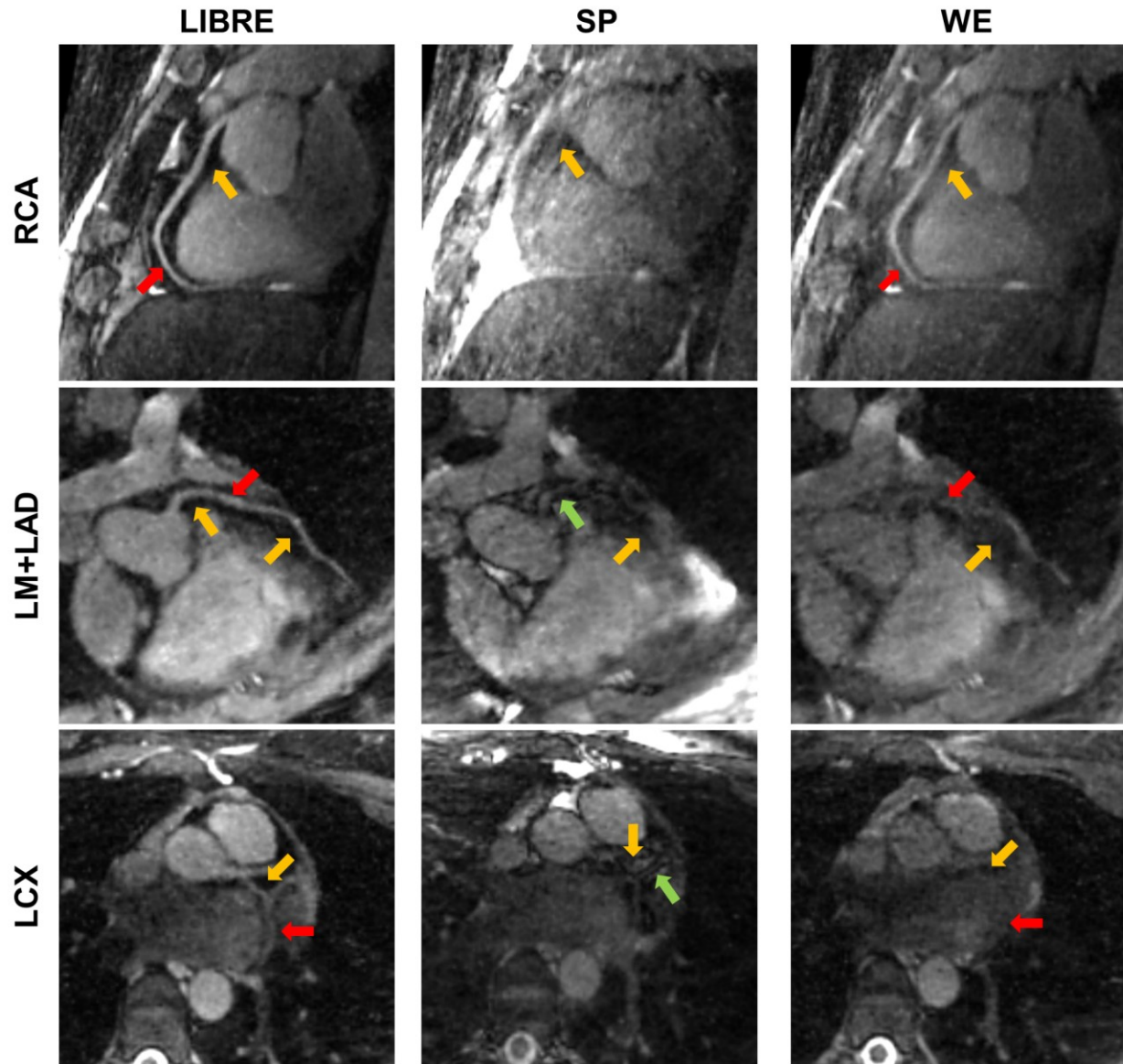
Figure 8. Comparison of non-interrupted free-running LIBRE images (LIBRE) with images using an ECG-triggered self-navigated fat-saturated T2-prepared 3D radial acquisition (FS) and images using the previously-published interrupted free-running acquisition (IFR) that is periodically interrupted by fat saturation and ramp-up pulses. Shown are reformatted images of the right coronary artery (RCA) and the left main and left anterior descending coronary artery (LM+LAD) acquired with the three sequences for two volunteers, A and B. Yellow arrows indicate regions of epicardial fat, and green arrows show water-fat phase cancellation artifacts.
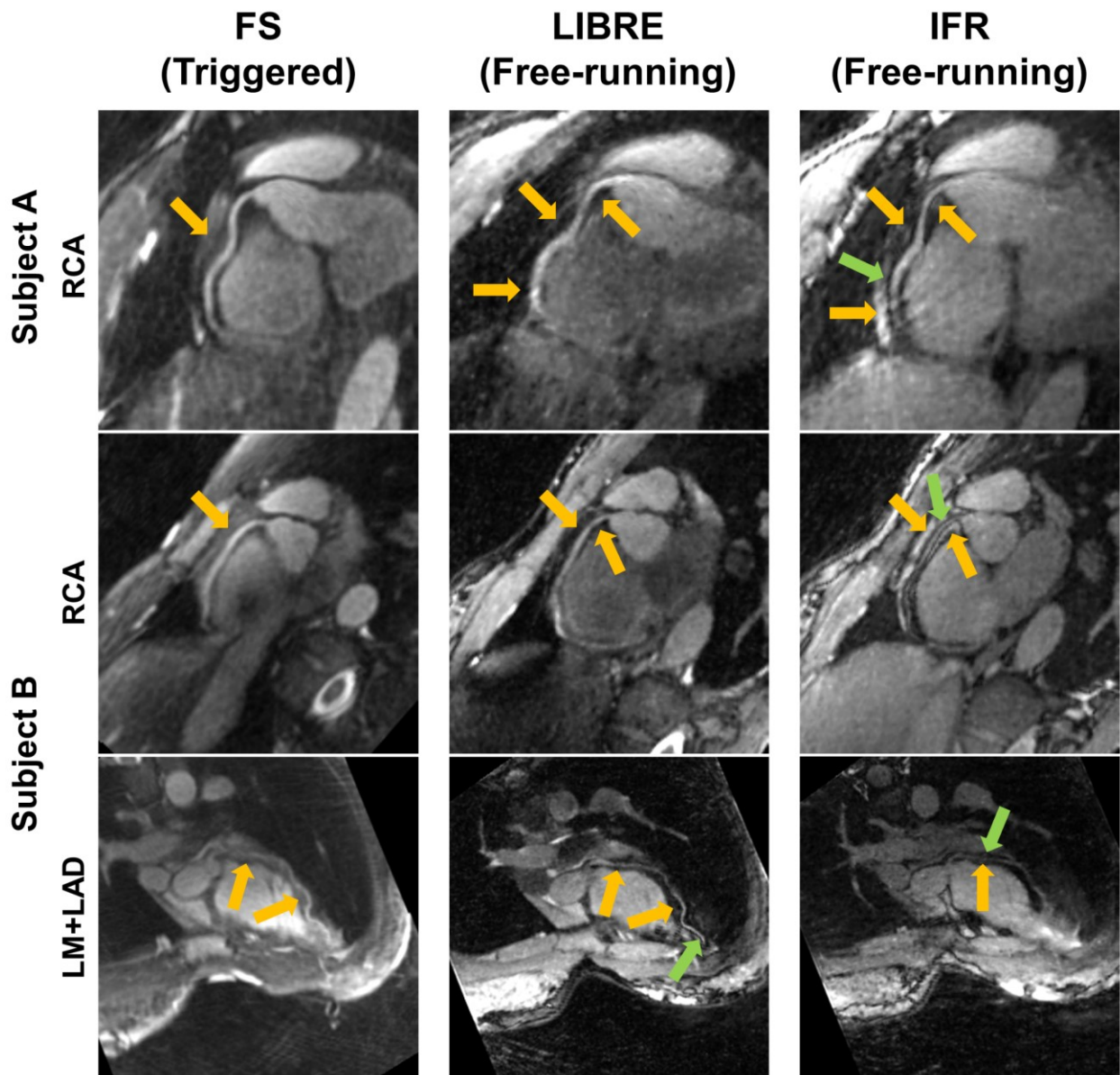
Supporting Information Video S1: Animations derived from one free-running LIBRE dataset showing respiratory motion at mid-diastole for one 3.5-mm-thick slice in transverse, coronal, and sagittal orientations. Epicardial fat was consistently suppressed, which allowed visualization of the coronary arteries, even though fat was not necessarily homogeneously suppressed throughout the field-of-view.

Supporting Information Video S2: Animation derived from one free-running LIBRE dataset showing cardiac motion at end-expiration for one 3.5-mm-thick slice in transverse, coronal, and sagittal orientations. Epicardial fat was consistently suppressed, which allowed visualization of the coronary arteries, even though fat was not necessarily homogeneously suppressed throughout the field-of-view.

Supporting Information Figure S1: Theoretical LIBRE signal behavior modelled using relaxation times measured in vivo. Transverse steady-state magnetization ($M_{ss}$), as a function of RF excitation angle and frequency (relative to the Larmor frequency) for different sub-pulse durations ($\tau$) of the LIBRE pulse, for blood, fat (6-peak model), myocardium, blood-fat contrast, and blood-myocardium contrast.
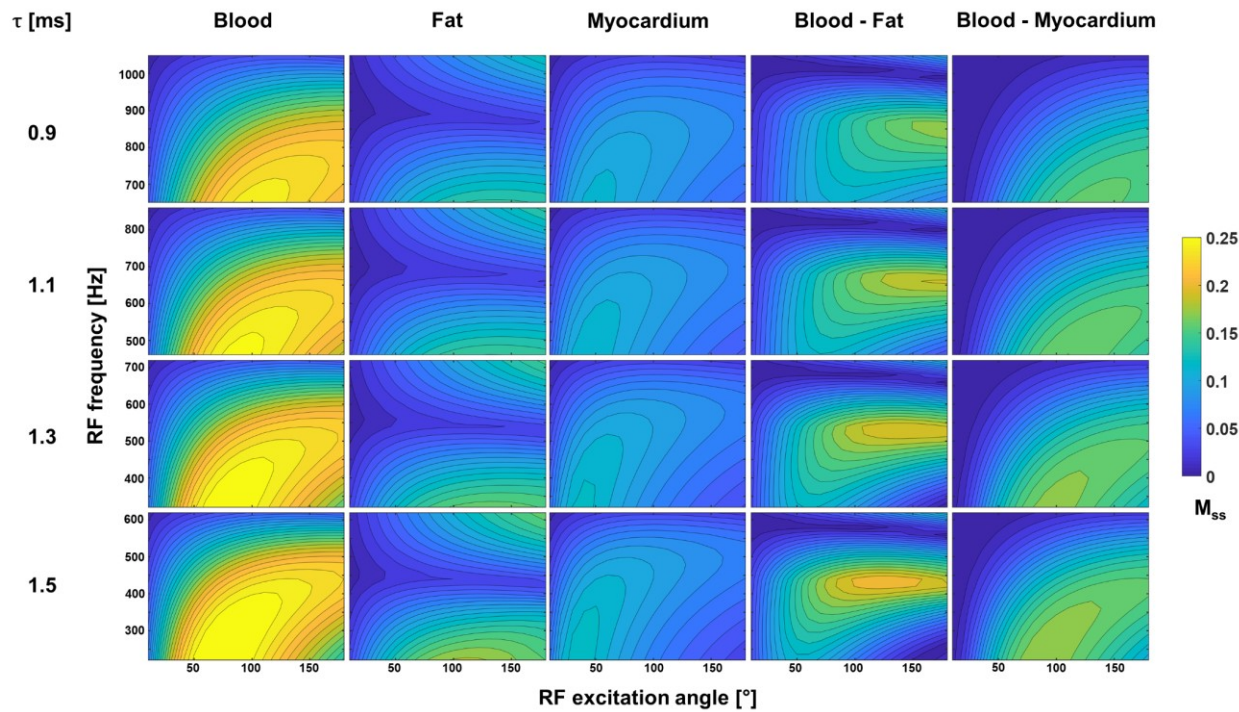
Supporting Information Figure S2: Theoretical LIBRE ($\tau$ = 1.3 ms, $f_{RF}$ = 540 Hz), SP, and WE signal behaviour modelled using relaxation times measured in vivo. Transverse steady-state magnetization ($M_{ss}$) as a function of RF excitation angle for A) blood, B) fat (6-peak model), C) myocardium, D) blood-fat contrast, and E) blood-myocardium contrast.